Optical coherence tomography angiography integrating differential phase and intensity images for *in vivo* imaging of a mouse retina

Fuwang Wu,[1,2] **Xiang He,**[1,2] **Yongjian Li,**[1,2] **Xiaoqi Lu,**[1,2] **Kaixuan Hu,**[1,2] **Hongtao Wei,**[1,2] **Wei Yi,**[1,2] **Yi Wan,**[1,2] **and Weiye Song**[1,2,*]

[1]*School of Mechanical Engineering, Shandong University, Jinan 250061, China*
[2]*Key Laboratory of High Efficiency and Clean Mechanical Manufacture of Ministry of Education, Shandong University, Jinan 250061, China*
*songweiye@sdu.edu.cn

Optical coherence tomography angiography (OCTA) suffers from more motion artifacts compared to optical coherence tomography, which are the primary source of image quality degradation in *in vivo* imaging. We propose an OCTA algorithm in this Letter that differs from motion compensation methods widely employed to reduce motion artifacts and effectively mitigates these artifacts. The algorithm integrates differential phase and intensity images based on the standard deviation of the flow signals. The performance of this algorithm is evaluated on mouse retina *in vivo* imaging. Compared to three conventional OCTA algorithms, the OCTA images obtained by the proposed algorithm exhibit fewer motion artifacts and less noise in tissue regions, with maximum improvements of 1.38 dB and 0.82 in signal-to-noise ratio and contrast-to-noise ratio (CNR), respectively, in the maximum projection of *en face* images. © 2025 Optica Publishing Group. All rights, including for text and data mining (TDM), Artificial Intelligence (AI) training, and similar technologies, are reserved.

Optical coherence tomography (OCT) is a noninvasive, three-dimensional imaging technique with micrometer resolution and has been widely used in the diagnosis of retinal diseases [1,2]. Optical coherence tomography angiography (OCTA) is a functional extension of OCT, developed to extract intrinsic blood flow signals within the microvasculature [3,4]. OCTA acquires microvascular images by detecting the change in signals induced by blood cell movement. To extract blood flow signals, various OCTA algorithms have been proposed. For example, speckle variance OCT (SVOCT) [5,6], phase variance OCT (PVOCT) [7,8], and optical microangiography (OMAG) [9,10] are widely used in *in vivo* microvasculature imaging, which are based on intensity, phase, and complex signals, respectively.

Since OCTA requires multiple scans at the same position, one of the major challenges in *in vivo* imaging is the motion artifacts caused by bulk motion phase shifts induced by breathing and heartbeats [11]. To reduce motion artifacts, various solutions have been proposed, such as algorithms combined with hardware design [12], motion compensation methods [13–15],

etc. The former can achieve more effective artifact suppression, while the need for hardware improvement may limit its application to certain OCT devices. There are two motion compensation methods that have been widely used to suppress motion artifacts. One method computes the motion-compensated phase by averaging phase shifts based on the A-line signal [14], while the other utilizes a velocity histogram along an A-line to calculate the compensated phase [15]. Wei *et al.* propose a bulk motion compensation method based on the standard deviation (STD) of phase-based OCTA and Doppler OCT flow signals to further enhance the accuracy of motion compensation and reduce computational load [16]. However, motion compensation methods need to calculate the bulk motion shift, which requires additional computations, and the effectiveness of motion artifact suppression depends on the estimation accuracy of the motion shift. Compared to motion compensation methods, enhancing the motion artifact suppression capability of OCTA algorithms may provide a superior solution.

In this Letter, we propose an OCTA algorithm that integrates differential phase and intensity standard deviation (DPISTD) of the flow signals. We found that calculating the standard deviation of the differential images can suppress motion artifacts and reduce noise in tissue regions. Then, integrating the standard deviation images of the differential phase and differential intensity images can further improve the quality of images. Effective motion artifact suppression was achieved without complex motion compensation calculations. To comprehensively investigate and present our algorithm, we compared our algorithm with three algorithms that utilize different forms of blood flow signals and are widely used in OCTA retinal imaging: SVOCT (intensity-based), PVOCT (phase-based), and OMAG (complex-based).

We performed *in vivo* imaging of a mouse retina using the OCT system previously established in the laboratory [17]. The system operated at 100 kHz A-line rate. The measured axial resolution was 2.3 μm, and the lateral resolution was estimated to be 10.9 μm. The exposure time was 9.2 μs. A raster scanning was used to acquire three-dimensional (3D) images centered at the optic disk. Each B-scan contained 400 A-lines. The B-scan was repeated five times for each slow scanning position, for a total of 512 positions and 2560 B-scans. The fast scanning was

performed in a sawtooth pattern, and its return time was set to 1/4 of the B-scan time. The experimental procedure was approved by the Institutional Animal Care and Use Committee (IACUC) of Shandong University.

We perform the OCT image reconstruction, including k-space interpolation, compensation for dispersion mismatch, and the fast Fourier transform [18]. Then, the complex dataset $C_{x,y,z,m}$ is obtained. x is the pixel coordinate in the fast scanning direction, y is the pixel coordinate in the slow scanning direction, z is the pixel coordinate in the depth direction of the image, and m is the time sequence of the B-scan acquired at the same scanning position.

The magnitudes of adjacent frames at the same scanning position are calculated, and the differential intensity (DI) image is obtained by differential operation between adjacent magnitudes of the complex data:

$$DI_{x,z,m} = |C_{x,z,m+1}| - |C_{x,z,m}|,\qquad(1)$$

where $|\cdot|$ is the absolute value of the complex data.

The differential phase image (DP image) is obtained as shown below:

$$DP_{x,z,m} = \tan^{-1}\left(\frac{\mathrm{Im}\left(C_{x,z,m+1}\cdot C^*_{x,z,m}\right)}{\mathrm{Re}\left(C_{x,z,m+1}\cdot C^*_{x,z,m}\right)}\right),\qquad(2)$$

where * denotes the conjugate of complex data. Then, the standard deviations of the DI images and the DP images derived from B-scans at the same scanning position are calculated separately (when $M \geq 3$):

$$IV_{x,y,z} = \sqrt{\frac{1}{M-1}\sum_{m=1}^{M-1}\left[DI_{x,z,m} - \frac{1}{M-1}\sum_{m=1}^{M-1}DI_{x,z,m}\right]^2},\quad(3)$$

$$PV_{x,y,z} = \sqrt{\frac{1}{M-1}\sum_{m=1}^{M-1}\left[DP_{x,z,m} - \frac{1}{M-1}\sum_{m=1}^{M-1}DP_{x,z,m}\right]^2},\quad(4)$$

where M is the number of repeated B-scans at the same scanning position. When $M = 2$, there is no meaningful standard deviation. $IV_{x,y,z}$ and $PV_{x,y,z}$ can be obtained by

$$IV_{x,y,z} = DI_{x,z,m},\qquad(5)$$

$$PV_{x,y,z} = DP_{x,z,m}.\qquad(6)$$

Finally, the DPISTD image can be obtained by calculating the square root of the product of the standard deviations derived from DP images and DI images:

$$DPI_{x,y,z} = \sqrt{PV_{x,y,z}\cdot IV_{x,y,z}}.\qquad(7)$$

The proposed algorithm is compared with SVOCT [5], PVOCT [7], and OMAG [9]. To reduce the motion artifacts, the global phase fluctuations were corrected by removing axial and lateral global phase fluctuations [11] in the phase-involved algorithms, DPISTD, PVOCT, and OMAG. Additionally, a threshold mask based on the averaged intensity image was multiplied by the phase difference images in DPISTD and PVOCT, to suppress random phase noise and improve blood vessel visualization

[7,19]. The threshold mask $M_{x,z,m}$ can be obtained by

$$M_{x,z,m} = |(C_{x,z,m+1}| + |C_{x,z,m}|)/2.\qquad(8)$$

The SNR [20,21] and contrast-to-noise ratio (CNR) [15,22] of OCTA images are calculated, which can be expressed as follows:

$$SNR = 20\log\frac{\bar{I}_{dynamic}}{\sigma_{static}},\qquad(9)$$

$$CNR = \frac{\bar{I}_{dynamic} - \bar{I}_{static}}{\sigma_{static}},\qquad(10)$$

where $\bar{I}_{dynamic}$ and $\bar{I}_{static}$ are the mean values of dynamic flow signals and static tissue signals, respectively, and σ_{static} is the standard deviation of the static tissue signals.

To ensure a fair visual comparison, the dynamic range of images was adjusted so that the same colormap can be used. The normalized image $I_{normalization}$ can be obtained by

$$I_{normalization} = \frac{x - \mu_x}{\sigma_x},\qquad(11)$$

where x is the pixel value of the image, μ_x is the mean value, and σ_x is the standard deviation of the pixels.

The OCTA *en face* images are binarized based on the threshold method to extract regions of blood vessels and tissues for the calculation of SNR and CNR. The threshold was calculated based on the Otsu method and then manually adjusted so that the vascular mask contained the vascular region as much as possible. To more effectively compare the ability of algorithms to visualize microvessels, the regions of large vessels were manually selected and subtracted from the blood vessel mask. The same masks were used for the calculation of SNR and CNR in all algorithms to ensure fairness and validity of the comparison.

The maximum projection images and the mean projection images obtained by the four algorithms are shown in Fig. 1. From Figs. 1(a)–1(d) and Figs. 1(e)–1(h), it can be observed that the mean projection images exhibit more motion artifacts and noise compared to the maximum projection images. But the mean projection images have higher SNR and lower CNR compared to the maximum projection images (Table 1). This may indicate that CNR is more suitable than SNR for the comparison of images acquired by different projection methods. Under the condition of using the same projection method, our algorithm achieves the highest values of both SNR and CNR. The motion artifacts induced by breathing (the white vertical lines marked by the arrows in Fig. 1(e)) are clearly evident in the SVOCT images, as this algorithm relies solely on the intensity information. Motion artifacts caused by heartbeats (the white vertical lines marked by the arrows in Fig. 1(f)) are even more pronounced in the PVOCT images. This is because PVOCT uses phase information to extract dynamic blood flow signals, which makes it more sensitive to phase shifts induced by the heartbeat. In contrast, OMAG, which is complex-based, has fewer motion artifacts than SVOCT and PVOCT. However, significant heartbeat-induced motion artifacts remain still present in the region near and above the optic nerve head (Fig. 1(g)). As shown in Fig. 1, SVOCT (intensity-based) can better suppress motion artifacts caused by breathing, and PVOCT (phase-based) can better reduce motion artifacts induced by heartbeats. By fusing intensity-based and phase-based OCTA and calculating the standard deviation of the differential images, motion artifacts induced by breathing and heartbeat are more effectively suppressed in the maximum
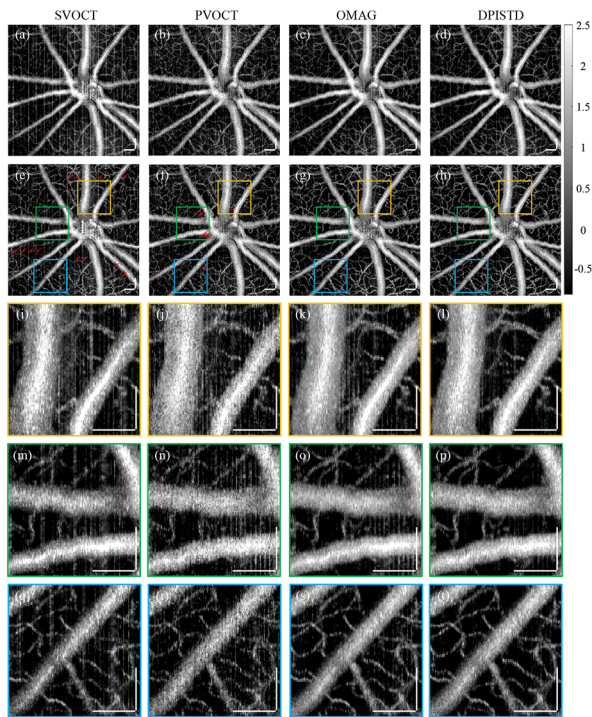
Fig. 1. OCTA *en face* images of the mouse retina. The first row shows the mean projection of OCTA *en face* images obtained by SVOCT, PVOCT, OMAG, and DPISTD, respectively. The second row shows the maximum projection images obtained by four algorithms. The third, fourth, and fifth rows show the enlarged images corresponding to the yellow, green, and blue boxes in (e)–(h), respectively. Scale bar = 100 μm.

Table 1. SNR and CNR of Maximum Projection Images and Mean Projection Images Obtained by the Four Algorithms

Algorithm	Maximum Projection		Mean Projection	
	SNR(dB)	CNR	SNR(dB)	CNR
SVOCT	15.23	2.34	16.29	1.60
PVOCT	15.28	2.40	15.40	1.85
OMAG	17.35	3.58	18.42	2.50
DPISTD	**18.73**	**4.40**	**19.28**	**2.93**

projection image of the DPISTD (Fig. 1(h)). As shown in the enlarged images (Figs. 1(i)–1(t)), the image obtained by DPISTD has fewer motion artifacts and less noise in the tissue regions.

To more fully compare the performance of the four algorithms, retinal data was post-processed and layered to obtain three laminar vascular/capillary plexuses, the superficial vascular plexus (SVP), intermediate capillary plexus (ICP), and deep capillary plexus (DCP) [23], as shown in Fig. 2.

The vascular signal region used for calculating the SNR and CNR of SVP images included the large vessel region. In contrast, for the calculation of the SNR and CNR of ICP and DCP images, the vascular signal region is selected to exclude the large vessel region. The results of SNR and CNR are presented in Table 2. The SNR and CNR of all vascular plexuses images obtained by DPISTD are at the highest values. Compared to the second-ranked OMAG, the SNR of the SVP image obtained by DPISTD is improved by 2.31 dB, and the CNR is increased by 3.02 in the maximum projection images. As shown in Fig. 2, the
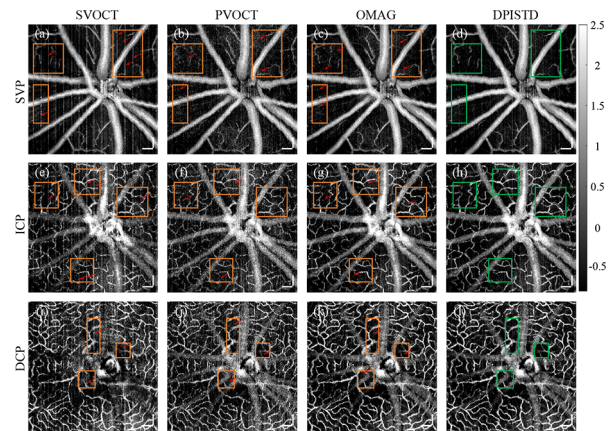

Fig. 2. Maximum projection images of three different retinal slabs obtained by different algorithms. The first row shows SVP, the second row shows ICP, and the third row shows DCP, obtained by SVOCT, PVOCT, OMAG, and DPISTD, respectively. In the regions marked by color boxes, motion artifacts and noise (marked by arrows) are reduced in the DPISTD images, which are noticeable and more in the images obtained by other algorithms. Scale bar = 100 μm.

Table 2. SNR and CNR of Three Different Retinal Slabs Obtained by the Four Algorithms

Retinal Slabs	Algorithm	Maximum Projection		Mean Projection	
		SNR(dB)	CNR	SNR(dB)	CNR
SVP	SVOCT	19.48	6.66	19.69	6.28
	PVOCT	18.71	6.10	18.49	5.69
	OMAG	20.97	8.11	21.56	8.15
	DPISTD	**23.28**	**11.13**	**23.23**	**10.33**
ICP	SVOCT	17.18	3.51	17.07	3.07
	PVOCT	16.00	3.26	15.57	2.97
	OMAG	19.42	5.18	19.03	4.34
	DPISTD	**20.15**	**5.80**	**19.66**	**4.89**
DCP	SVOCT	18.25	4.19	18.00	3.10
	PVOCT	17.43	3.87	16.72	3.12
	OMAG	20.32	5.99	19.83	4.30
	DPISTD	**20.57**	**6.24**	**20.01**	**4.57**

vascular plexus images obtained by the DPISTD have fewer motion artifacts and less tissue noise, which are noticeable in SVP and DCP images.

The number of repeated frames is a critical parameter in OCTA [18]. Therefore, the OCTA images and their SNR and CNR, obtained by each algorithm at different numbers of frames, are compared and analyzed, as shown in Fig. 3 and Fig. 4. Although the SNR of DPISTD is comparable to that of SVOCT when the number of repeated frames is two, the CNR of DPISTD is significantly higher than that of SVOCT. This indicates that the structural contrast of the DPISTD images is superior. When the number of repeated frames is 3, 4, and 5, the SNR and CNR of the maximum projection images and the mean projection images obtained by DPISTD are all at the highest and show a significant improvement compared to the second-ranked algorithm.

In order to better show the advantages of DPISTD, we only show the maximum projection images obtained by DPISTD and OMAG (the second-ranked algorithm) in Fig. 4. As shown in Fig. 4, the OCTA images obtained by OMAG have more motion artifacts (marked by arrows) compared to DPISTD when the number of frames is 2, 3, 4, and 5. When $M = 5$, there are still many motion artifacts in Fig. 4(n). The motion artifacts
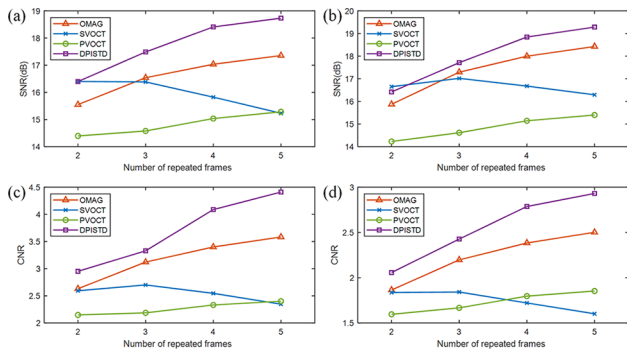
Fig. 3. SNR and CNR of the maximum projection images and mean projection images obtained by the four algorithms as the number of repeated frames is increased. (a) and (b) are the SNR of maximum projection images and mean projection images obtained by different algorithms, respectively. (c) and (d) are the CNR of maximum projection images and mean projection images.
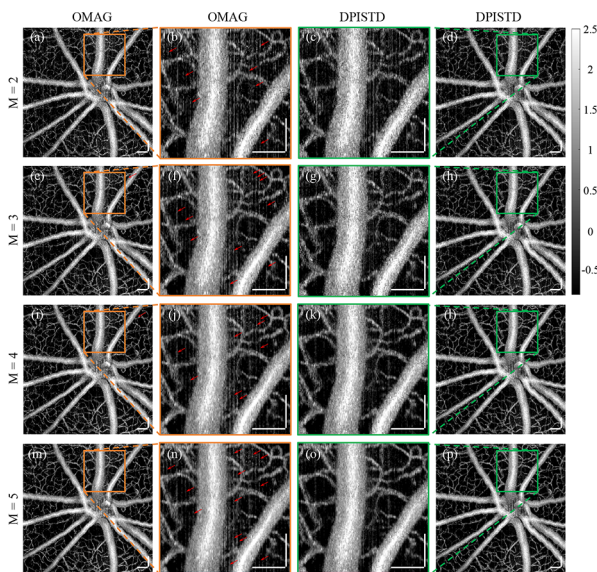

Fig. 4. Maximum projection images obtained by the DPISTD and OMAG for different numbers of repeated frames. Scale bar = 100 μm.

and noise in the DPISTD images are gradually reduced as the number of frames increases. The contrast of the capillaries in DPISTD images is improved significantly, as shown in Figs. 4(c) and 4(o).

When $M = 2$, OCTA images (Figs. 4(c) and 4(d)) were obtained using Eqs. (5) and (6) without calculating the standard deviation. When $M = 3$, two differential images can be obtained, and then the standard deviation of these two images was calculated to obtain the OCTA images (Figs. 4(g) and 4(h)). Compared to Fig. 4(c), motion artifacts are significantly reduced in Fig. 4(g). When the number of frames continues to increase, the suppression of motion artifacts is no longer so obvious. This can account for the motion artifact suppression effect of the calculation of the standard deviation. This may be attributed to the rhythmic and regular nature of the mouse's breathing and heartbeat, which results in their movements being approximately linear or uniformly variable [11], and the motion artifact signals also vary approximately uniformly compared to the random blood flow signal. Therefore, the differential signals of

motion artifacts between adjacent images are similar, and their standard deviation is small. In contrast, blood flow signals vary randomly, leading to a large standard deviation in their differential signals. As a result, the signals in the static tissue region are suppressed, and the blood flow signals are enhanced, thus improving the performance of the angiography algorithm.

In this Letter, we propose an OCTA algorithm that integrates differential phase and intensity images based on the STD of the flow signals. The performance of the algorithm is demonstrated on OCTA *in vivo* imaging of the mouse retina. Quantitative and qualitative analyzes are performed, comparing the proposed algorithm with three other algorithms: SVOCT, PVOCT, and OMAG. The different laminar vascular/capillary plexuses and the OCTA *en face* images at different numbers of repeated frames are compared and analyzed. The results demonstrate that the proposed algorithm can more effectively suppress motion artifacts and has less noise in the tissue regions.

Disclosures. The authors declare no conflicts of interest.

Data availability. Data underlying the results presented in this Letter are not publicly available at this time but may be obtained from the authors upon reasonable request.

REFERENCES

1. D. Huang, E. A. Swanson, C. P. Lin, *et al.*, Science **254**, 1178 (1991).
2. P. L. Nesper, B. T. Soetikno, H. F. Zhang, *et al.*, Vision Res. **139**, 191 (2017).
3. R. F. Spaide, J. G. Fujimoto, N. K. Waheed, *et al.*, Prog. Retin Eye Res. **64**, 1 (2018).
4. Y. Jia, O. Tan, J. Tokayer, *et al.*, Opt. Express **20**, 4710 (2012).
5. A. Mariampillai, B. A. Standish, E. H. Moriyama, *et al.*, Opt. Lett. **33**, 1530 (2008).
6. A. Mariampillai, M. K. Leung, M. Jarvi, *et al.*, Opt. Lett. **35**, 1257 (2010).
7. J. Fingler, R. J. Zawadzki, J. S. Werner, *et al.*, Opt. Express **17**, 22190 (2009).
8. D. Y. Kim, J. Fingler, J. S. Werner, *et al.*, Biomed. Opt. Express **2**, 1504 (2011).
9. R. K. Wang and S. Hurst, Opt. Express **15**, 11402 (2007).
10. H. L. Rao, S. Dasari, N. K. Puttaiah, *et al.*, J. Glaucoma **34**, 175 (2025).
11. J. Lee, V. Srinivasan, H. Radhakrishnan, *et al.*, Opt. Express **19**, 21258 (2011).
12. S. Y. Ksenofontov, P. Shilyagin, D. Terpelov, *et al.*, Instrum. Exp. Tech. **66**, 1037 (2023).
13. X. Wei, T. T. Hormel, Y. Guo, *et al.*, Biomed. Opt. Express **11**, 3234 (2020).
14. V. X. Yang, M. L. Gordon, B. Qi, *et al.*, Opt. Express **11**, 794 (2003).
15. J. Xu, S. Song, Y. Li, *et al.*, Phys. Med. Biol. **63**, 015023 (2017).
16. X. Wei, A. Camino, S. Pi, *et al.*, Opt. Lett. **43**, 2204 (2018).
17. W. Yi, K. Hu, Y. Wan, *et al.*, J. Lumin. **270**, 120550 (2024).
18. W. Song, W. Shao, W. Yi, *et al.*, Biomed. Opt. Express **11**, 4037 (2020).
19. W. Shi, C. Chen, C. R. Pasarikovski, *et al.*, Appl. Opt. **58**, 3401 (2019).
20. R. K. Wang, A. Zhang, W. J. Choi, *et al.*, Opt. Lett. **41**, 2330 (2016).
21. X. Chen, Z. Ma, C. Wang, *et al.*, J. Biophotonics **17**, e202400198 (2024).
22. I. Gorczynska, J. V. Migacz, R. J. Zawadzki, *et al.*, Biomed. Opt. Express **7**, 911 (2016).
23. T.-H. Kim, T. Son, Y. Lu, *et al.*, Trans. Vis. Sci. Tech. **7**, 42 (2018).